Intervalley Band Crossing and Transition of Fractional Chern Insulators in Floquet Twisted Bilayer $MoTe_2$

Yuhao Shi(石宇昊)[1] and Zhao Liu(刘钊)[1,2*]

[1]*Zhejiang Institute of Modern Physics, Zhejiang University, Hangzhou 310058, China*
[2]*Zhejiang Key Laboratory of Micro-Nano Quantum Chips and Quantum Control, School of Physics, Zhejiang University, Hangzhou 310027, China*

(Received 15 January 2026; accepted manuscript online 17 April 2026)

We study the twisted $MoTe_2$ homobilayer coupled to periodic driving of a circularly polarized light (CPL). Using Floquet theory in the high-frequency limit, we start from the Dirac model including both the valence and conduction bands of monolayer $MoTe_2$ to derive an effective time-independent Floquet Hamiltonian. The photon processes coupling the valence and conduction bands are captured in this Floquet analysis, and the resulting Floquet Hamiltonian contains explicit time-reversal symmetry breaking terms that are absent if conduction bands are integrated out from the beginning of the derivation. Based on the Floquet Hamiltonian, we find the increase of CPL driving intensity can cause the crossing of Floquet bands and redistribution of holes between the two valleys. When interactions are included, a transition between Floquet Laughlin-type fractional Chern insulators with different behaviors of valley polarization is identified at total hole filling 5/3.

DOI: 10.1088/0256-307X/43/5/050716 CSTR: 32039.14.0256-307X.43.5.050716

1. Introduction. Floquet systems have emerged as a versatile platform for engineering novel states of quantum matter. By subjecting materials to periodic driving, one can dynamically modify their band structures and effective interactions, enabling topological phases and dynamical transitions that are inaccessible in equilibrium.[1–6] These effects are typically described by an effective static Floquet Hamiltonian, obtained through high-frequency expansions[7–9] or more general non-perturbative approaches.[10–15] Over the past decade, this framework has been widely applied to both weakly and strongly correlated systems, highlighting Floquet engineering as a promising route to control quantum phases.[16–19]

This framework has been naturally extended to moiré materials, which provide a fertile setting for exploring the interplay between strong correlations and topology. For example, circularly polarized light (CPL) shining vertically across the twisted multilayer graphene has been shown to cause nontrivial modifications of the band topology,[12,17,20–27] which can potentially support fractional Chern insulators (FCIs),[28–35] the lattice analogs of the celebrated fractional quantum Hall effect, in Floquet systems.[36–38] Advances have also been reported in twisted $MoTe_2$ homobilayers ($tMoTe_2$),[39,40] which host flat bands over a wide range of twist angles.[41–43] Unlike in twisted multilayer graphene, recent work focusing on the valence bands of $tMoTe_2$ found that the leading effect of the vertically applied high-frequency CPL is only a constant overall quasienergy shift of the static bands.[44] This shift is independent of valley and driving frequency Ω. Nevertheless, topological transitions can be driven by longitudinal light generated in a waveguide.[44]

The valence and conduction band edges near the K and K' points of monolayer $MoTe_2$ are well described by massive Dirac fermions.[45] In previous works on $tMoTe_2$, this massive Dirac structure is mostly neglected by perturbatively dropping the conduction band, which is separated from the valence band by a large gap, resulting in a free-electron description (parabolic dispersion) of the valence band edge of monolayer $MoTe_2$. While this approximation works well for describing the band dispersion, it fails to capture the feature of time-reversal symmetry breaking in the original massive Dirac model,[46] which may manifest itself under the driving of CPL. This observation motivates us to revisit the Floquet problem in $tMoTe_2$ using the full consideration of the massive Dirac structure in monolayers. It is also interesting to ask whether Floquet FCIs induced by CPL exist in $tMoTe_2$ when interactions are included.

In this work, we investigate the off-resonant high-frequency Floquet engineering of $tMoTe_2$ by vertical CPL shining. Instead of adopting the free-electron model for each $MoTe_2$ monolayer from the beginning, we start from the massive Dirac model to derive the effective Floquet Hamiltonian and integrate out the conduction band only at the end. This method allows us to capture the photon processes coupling the valence and conduction bands. In the obtained free-electron approximation of the Floquet Hamiltonian, we identify overall quasienergy shifts that depend not only on the driving frequency but also on the valley. This time-reversal symmetry breaking feature is

*Corresponding author. Email: zhaol@zju.edu.cn
© 2026 Chinese Physical Society and IOP Publishing Ltd. All rights, including for text and data mining, AI training, and similar technologies, are reserved.

absent if one derives the Floquet Hamiltonian completely within the free-electron framework. We then incorporate the screened Coulomb interaction into the system and confirm that it does not introduce additional interaction terms in the second-order $(1/\Omega^2)$ corrections of the Floquet Hamiltonian that may affect the many-body physics of the driven system. By performing exact diagonalization of the many-body Floquet Hamiltonian at total hole filling $\nu_{\rm h} = 5/3$, we track the evolution of the ground state of the Floquet Hamiltonian when increasing CPL intensity drives the crossing of Floquet bands in opposite valleys, revealing the competition between Floquet Laughlin-type FCI phases with different behaviors of valley polarization.

2. Dirac Model of Static tMoTe$_2$. We start our discussion from the single-particle Hamiltonian of the static tMoTe$_2$. We assume that the top and bottom layers are rotated by $\pm\theta/2$ from the AA stacked configuration. The moiré Hamiltonian in the framework of massive Dirac model takes the form of[45,47]

$$\mathcal{H}_{\rm kin} = \begin{pmatrix} h_{{\rm t},+} & T_+ \\ T_+^\dagger & h_{{\rm b},+} \end{pmatrix} \bigoplus \begin{pmatrix} h_{{\rm t},-} & T_- \\ T_-^\dagger & h_{{\rm b},-} \end{pmatrix}, \tag{1}$$

where $h_{\ell,\xi}$ is the massive Dirac Hamiltonian of layer ℓ at the valley $\xi = \pm$ (K and K'), and T_ξ is the interlayer hopping matrix. Throughout this work, the layer index ℓ takes the values ${\rm t} = +1$ and ${\rm b} = -1$ for the top and bottom layers, respectively. The monolayer term $h_{\ell,\xi}$ includes both the conduction and valence band edges in valley ξ, as given by[45]

$$\begin{aligned} &h_{\ell,\xi}(\boldsymbol{k},\boldsymbol{r}) \\ &= \begin{pmatrix} \Delta_{\rm g} + \Delta_{\ell,{\rm c}}(\boldsymbol{r}) & 0 \\ 0 & \Delta_{\ell,{\rm v}}(\boldsymbol{r}) \end{pmatrix} + \exp\left(+{\rm i}\ell\xi\frac{\theta}{4}\sigma_z\right) \\ &\times \left[\hbar v_{\rm F}\delta\boldsymbol{k}_\xi^\ell \cdot (\xi\sigma_x, \sigma_y)\right] \exp\left(-{\rm i}\ell\xi\frac{\theta}{4}\sigma_z\right), \end{aligned} \tag{2}$$

where the subscripts "c" and "v" denote the conduction and valence bands, respectively, $\Delta_{\rm g} \approx 1.1\,{\rm eV}$ is the average band gap, and $v_{\rm F}$ is the Fermi velocity. We assume that the electron's spin in the Dirac model is polarized to opposite directions in the two valleys (spin-valley locking), which is caused by the strong spin–orbit coupling at the valence band edge and the absence of spin flipping effects at the conduction band edge.[45] The relative momentum $\delta\boldsymbol{k}_\xi^\ell = (\boldsymbol{k} - \boldsymbol{\kappa}_{\ell,\xi})$, with $\boldsymbol{\kappa}_{\ell,\xi}$ being the valley ξ of layer ℓ. $\Delta_{\ell,p}$ measures the variation of the extrema energy in band $p = {\rm c}, {\rm v}$ as a function of position $\boldsymbol{r}$, and takes the form of

$$\Delta_{\ell,p}(\boldsymbol{r}) = 2V_p \sum_{j=1}^{3} \cos(\boldsymbol{b}_{2j-1} \cdot \boldsymbol{r} - \ell\psi_p). \tag{3}$$

Here $\boldsymbol{b}_n = \frac{4\pi}{\sqrt{3}a_0/\theta} R_z(\frac{n-1}{3}\pi)\hat{x}$ are the moiré reciprocal lattice vectors, R_z generates a counterclockwise rotation around the z-axis, and $a_0 \approx 3.52\,$Å is the lattice constant of monolayer MoTe$_2$. The interlayer tunneling T_ξ in valley ξ is parametrized as

$$\begin{aligned} &T_\xi(\boldsymbol{r}) \\ &= \begin{pmatrix} w_{\rm c} & w_{\rm cv} \\ w_{\rm vc} & w_{\rm v} \end{pmatrix} \\ &+ \begin{pmatrix} w_{\rm c} & w_{\rm cv}\exp(-{\rm i}2\xi\pi/3) \\ w_{\rm vc}\exp({\rm i}2\xi\pi/3) & w_{\rm v} \end{pmatrix} \exp({\rm i}\xi\boldsymbol{b}_2 \cdot \boldsymbol{r}) \\ &+ \begin{pmatrix} w_{\rm c} & w_{\rm cv}\exp({\rm i}2\xi\pi/3) \\ w_{\rm vc}\exp(-{\rm i}2\xi\pi/3) & w_{\rm v} \end{pmatrix} \exp({\rm i}\xi\boldsymbol{b}_3 \cdot \boldsymbol{r}). \end{aligned} \tag{4}$$

3. Floquet Engineering. In the following, we include the effect of the vertically applied CPL driving in the single-particle physics by applying the Peierls substitution $\boldsymbol{k} \to \boldsymbol{k} + e\boldsymbol{A}/\hbar$ with the vector potential $\boldsymbol{A} = A_0(\cos\Omega t, -\sin\Omega t)$ in Eq. (2). The light field is represented by an in-plane electric field $\boldsymbol{E} = -\partial\boldsymbol{A}/\partial t$. Here A_0 measures the driving strength and Ω is the driving frequency. Then Eq. (1) is modified to a time-dependent single-particle Hamiltonian $\mathcal{H}_{\rm kin}(t)$. Note that we keep the interlayer tunneling as in the static case, because it is dominated by hopping between atoms that are exactly on top of each other, thus mostly contributed by the z-component of the vector potential which is absent in our setup. Because the light driving does not flip spin, the electron's spin is still polarized in each valley after the CPL is applied.

According to the Floquet theory, the stroboscopic evolution of the system can be captured by a time-independent effective Floquet Hamiltonian $H_{\rm eff}$ (upon a unitary transformation from micromotion).[7,8,48,49] At high frequencies, $H_{\rm eff}$ can be represented by a series expansion of $1/\Omega$:

$$H_{\rm eff} \approx H_{\rm eff}^{(0)} + H_{\rm eff}^{(1)} + H_{\rm eff}^{(2)}, \tag{5}$$

where we keep to the second order. We use $H_m = (1/T)\int_0^T \mathcal{H}_{\rm kin}(t)\exp(-{\rm i}m\Omega t){\rm d}t$ to denote the Fourier component of $\mathcal{H}_{\rm kin}(t)$. In our setup, H_m is nonzero only if $m = 0, \pm 1$. Using the Magnus expansion,[7,8,48,49] we obtain

$$H_{\rm eff}^{(0)} = H_0 = \mathcal{H}_{\rm kin}, \tag{6a}$$

$$H_{\rm eff}^{(1)} = \frac{1}{\hbar\Omega}[H_1, H_{-1}] = \frac{(ev_{\rm F}A_0)^2}{\hbar\Omega}\sigma_z \otimes \mathbb{1}_2^\ell \otimes \xi_z, \tag{6b}$$

$$\begin{aligned} H_{\rm eff}^{(2)} &= \frac{1}{2(\hbar\Omega)^2}[H_1,[H_0,H_{-1}]] + {\rm h.c.} \\ &= \frac{(ev_{\rm F}A_0)^2}{(\hbar\Omega)^2}\Bigg[-\mathcal{H}_{\rm kin} + \frac{\Delta_{\ell,{\rm v}}}{2}(\mathbb{1}_2^p + \sigma_z) \otimes \mathbb{1}_2^\ell \otimes \mathbb{1}_2^\xi \\ &+ \frac{\Delta_{\rm g} + \Delta_{\ell,{\rm c}}}{2}(\mathbb{1}_2^p - \sigma_z) \otimes \mathbb{1}_2^\ell \otimes \mathbb{1}_2^\xi \\ &+ T' \otimes \frac{\gamma_x + {\rm i}\gamma_y}{2} \otimes \mathbb{1}_2^\xi \\ &+ (T')^\dagger \otimes \frac{\gamma_x - {\rm i}\gamma_y}{2} \otimes \mathbb{1}_2^\xi \Bigg], \end{aligned} \tag{6c}$$

where $\mathbb{1}_2^p$, $\mathbb{1}_2^\ell$, and $\mathbb{1}_2^\xi$ are 2×2 identity matrices in the band, layer, and valley spaces, respectively, σ_i and γ_i ($i = x, y, z$) are Pauli matrices in the band and

layer spaces, respectively, and $T'_\xi(\boldsymbol{r}) = \mathrm{diag}(w_\mathrm{v}\exp(\mathrm{i}\xi\theta), w_\mathrm{c}\exp(-\mathrm{i}\xi\theta))(1+\exp(\mathrm{i}\xi\boldsymbol{b}_2\cdot\boldsymbol{r})+\exp(\mathrm{i}\xi\boldsymbol{b}_3\cdot\boldsymbol{r}))$. Combining these terms together, we have

$$H_\mathrm{eff} = h'_{\ell,\xi}(\boldsymbol{k},\boldsymbol{r})\otimes\mathbb{1}_2^\ell\otimes\mathbb{1}_2^\xi + \left\{\Delta_T^\xi(\boldsymbol{r})\otimes\left(\frac{\gamma_x+\mathrm{i}\gamma_y}{2}\right)+\mathrm{h.c.}\right\}\otimes\mathbb{1}_2^\xi, \quad (7)$$

with

$$h'_{\ell,\xi}(\boldsymbol{k},\boldsymbol{r}) = \left(1-\frac{\Delta}{\hbar\Omega}\right)\left\{\begin{pmatrix}\Delta_\mathrm{g}+\Delta_{\ell,\mathrm{c}}(\boldsymbol{r}) & 0\\ 0 & \Delta_{\ell,\mathrm{v}}(\boldsymbol{r})\end{pmatrix} + \exp\left(+\mathrm{i}\ell\xi\frac{\theta}{4}\sigma_z\right)\left[\hbar v_\mathrm{F}\delta\boldsymbol{k}_\xi^\ell\cdot(\xi\sigma_x,\sigma_y)\right] \times\exp\left(-\mathrm{i}\ell\xi\frac{\theta}{4}\sigma_z\right)\right\} + \left(\xi-\frac{\Delta_\mathrm{g}}{\hbar\Omega}\right)\Delta\cdot\sigma_z + \frac{\Delta}{\hbar\Omega}\begin{pmatrix}\Delta_\mathrm{g}+\Delta_{\ell,\mathrm{v}}(\boldsymbol{r}) & 0\\ 0 & \Delta_{\ell,\mathrm{c}}(\boldsymbol{r})\end{pmatrix}, \quad (8a)$$

$$\Delta_T^\xi(\boldsymbol{r}) = T_\xi(\boldsymbol{r}) + \frac{\Delta}{\hbar\Omega}[T'_\xi(\boldsymbol{r})-T_\xi(\boldsymbol{r})]. \quad (8b)$$

Here we have used $\Delta = (ev_\mathrm{F}A_0)^2/(\hbar\Omega)$ to denote the intensity of CPL driving. We will fix $\hbar\Omega = 3\,\mathrm{eV}$ in the remainder of this paper. This driving frequency can be readily realized by ultraviolet light. In the Supplementary Materials (SM), we will show that the light driving at this frequency is off-resonant and the high-frequency Magnus expansion truncated at the order of $1/\Omega^2$ indeed well captures the quasienergy bands.

The Floquet Hamiltonian Eq. (5) keeps both the valence and conduction bands of the monolayer $MoTe_2$. For comparison with the undriven case in which the free-electron model involving the valence bands only was extensively used in previous studies, we perform the Schrieffer–Wolff transformation to Eq. (7) to integrate out the conduction bands. With some further simplifications, we finally obtain a Floquet Hamiltonian $\tilde{H}_\mathrm{eff}$ for the valence bands under the free-electron approximation, which takes a very similar form to that in the undriven case.[47] The intralayer part of $\tilde{H}_\mathrm{eff}$ is

$$\tilde{h}_{\ell,\xi}(\boldsymbol{k},\boldsymbol{r}) = -\frac{\hbar^2\delta\boldsymbol{k}_\xi^{\ell\,2}}{2m^*}+\Delta_{\ell,v}(\boldsymbol{r})+\left(-\xi+\frac{\Delta_\mathrm{g}}{\hbar\Omega}\right)\Delta, \quad (9)$$

where the valley-dependent effective mass is $m^* = [\Delta_\mathrm{g} + 2(\xi-\Delta_\mathrm{g}/\hbar\Omega)\Delta]/(2v_\mathrm{F}^2)$. The interlayer tunneling term is

$$\tilde{T}_\xi(\boldsymbol{r}) = w_\mathrm{v}(1+\exp(\mathrm{i}\xi\boldsymbol{b}_2\cdot\boldsymbol{r})+\exp(\mathrm{i}\xi\boldsymbol{b}_3\cdot\boldsymbol{r})). \quad (10)$$

The details of our derivation are presented in the SM.

In Fig. 1, we present the first two moiré valence bands in the two valleys, obtained for the static $tMoTe_2$, the full Floquet Hamiltonian H_eff, and the valence-band Floquet Hamiltonian $\tilde{H}_\mathrm{eff}$, using the parameters $\Delta_\mathrm{g} = 1.1\,\mathrm{eV}$, $v_\mathrm{F} = 0.4\times10^6\,\mathrm{ms}^{-1}$, $w_\mathrm{cv} = 15.3\,\mathrm{meV}$, $(V_\mathrm{v},\psi_\mathrm{v},w_\mathrm{v}) = (8\,\mathrm{meV},-89.6^\circ,-8.5\,\mathrm{meV})$, $(V_\mathrm{c},\psi_\mathrm{c},w_\mathrm{c}) = (5.97\,\mathrm{meV},-87.9^\circ,-2\,\mathrm{meV})$,[47] and $\Delta = 10\,\mathrm{meV}$. One can see that the quasienergy spectra of H_eff and $\tilde{H}_\mathrm{eff}$ are indeed very similar to each other, which justifies our

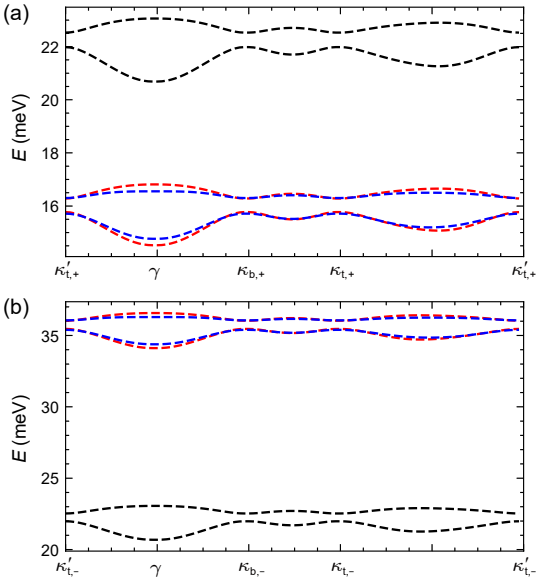

Fig. 1. The first two moiré valence bands in the two valleys along a high-symmetry path in the moiré Brillouin zone at a twist angle of 1.2°. (a) The bands in valley +. (b) The bands in valley −. Black dashed lines represent the undriven $tMoTe_2$ described by the massive Dirac model. Red and blue dashed lines correspond to the quasienergies of the full Floquet Hamiltonian H_eff and the valence-band Floquet Hamiltonian $\tilde{H}_\mathrm{eff}$, respectively. The intensity of CPL is chosen as $\Delta = 10\,\mathrm{meV}$.

Schrieffer–Wolff transformation of integrating out the conduction bands. We will use the valence-band Floquet Hamiltonian $\tilde{H}_\mathrm{eff}$ in what follows.

From Fig. 1, we can see that the dispersion of valence bands remains largely unchanged under periodic driving compared to the static case, except for an overall shift whose leading term $-\xi\Delta$ is in the order of $1/\Omega$ and is opposite in different valleys [Eq. (9)]. This feature (as well as the valley-dependent effective mass) demonstrates the time-reversal symmetry breaking under the driving of CPL. Notably, this symmetry breaking signal is absent in the Floquet Hamiltonian derived within the free-electron framework[44] (also shown in the SM), but could appear in the effective tight-binding description of the driven monolayer $MoTe_2$.[39] The necessity of including the conduction bands at the beginning of the Floquet analysis stems from the presence of photon processes coupling the valence and conduction bands, which can be seen in the nonzero matrix elements of $H_{\pm1}$ between the valence and conduction band states (see the SM). If the static conduction bands are already integrated out before the Floquet analysis is performed, these processes cannot be captured.

The almost opposite quasienergy shift in the two valleys of driven $tMoTe_2$ immediately indicates that light can play the role of a pseudospin Zeeman field and cause the crossing between Floquet bands of different valleys. In Fig. 2, we present the Floquet band structures at CPL intensity $\Delta = 5\,\mathrm{meV}$, $10.3\,\mathrm{meV}$, and $15\,\mathrm{meV}$. With increasing Δ, the top Floquet valence band of valley + crosses with the second Floquet valence band of valley −. Such

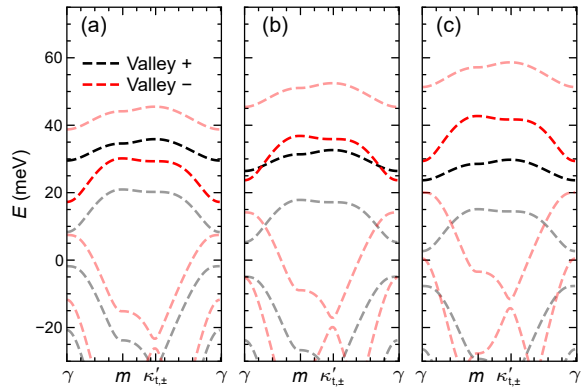

Fig. 2. The Floquet band structures at CPL intensity (a) $\Delta = 5\,\text{meV}$, (b) 10.3 meV, and (c) 15 meV. The two crossing bands—the top valence band of valley + and the second valence band of valley − —are highlighted by dark colors.

a crossing at the single-particle level will induce redistribution of electrons in the two valleys and could lead to interesting phase transitions of many-body physics in the driven system.

4. Many-Body Physics. Now we will explore the many-body physics in driven $tMoTe_2$ that happens during the Floquet band crossing shown in Fig. 2. The first step is to derive the many-body Floquet Hamiltonian with electron–electron interactions taken into account. For undriven $tMoTe_2$, the dual-gate screened Coulomb interaction

$$\mathcal{H}_{\text{int}} = \frac{1}{2}\sum_{\boldsymbol{q}} V(\boldsymbol{q}) : \rho(\boldsymbol{q})\rho(-\boldsymbol{q}) : \tag{11}$$

between electrons is often adopted, where $\rho(\boldsymbol{q}) = \sum_j \exp(\mathrm{i}\boldsymbol{q}\cdot\boldsymbol{r}_j)$ is the density operator and :: means the normal ordering. The Fourier transform of the interaction potential is

$$V(\boldsymbol{q}) = \frac{e^2}{4\pi\epsilon_0\epsilon_{\text{r}}}\frac{2\pi}{|\boldsymbol{q}|}\tanh|\boldsymbol{q}|d, \tag{12}$$

where ϵ_0 is the vacuum permittivity, ϵ_{r} is the relative dielectric constant, and d is the distance from a gate to the sample. The two valleys are decoupled at the single-electron level. Moreover, $V(\boldsymbol{q})$ decays fast with increasing $|\boldsymbol{q}|$, so we neglect the intervalley scattering which requires large momentum transfer. Then we have conserved particle number in each valley and $\rho(\boldsymbol{q}) = \sum_\xi \rho_\xi(\boldsymbol{q})$, where $\rho_\xi(\boldsymbol{q})$ is the density operator of electron in valley ξ. After the CPL driving is switched on, the interaction remains as in the undriven case since it has the density–density form. Therefore, regarding the Floquet Hamiltonian in the presence of the interaction, we need to add $\mathcal{H}_{\text{int}}$ to $H_{\text{eff}}^{(0)}$ in Eq. (5), but $H_{\text{eff}}^{(1)}$ is not altered. However, there is still a subtle thing: new terms could appear in $H_{\text{eff}}^{(2)}$ due to the possible contribution from $[H_1, [\mathcal{H}_{\text{int}}, H_{-1}]]$.[37] Fortunately, after carefully calculating this commutator, we find it is exactly zero, as in driven TBG.[38] Then the total many-body Floquet Hamiltonian $\tilde{H}_{\text{eff}}^{\text{mb}}$ truncated at the order of $1/\Omega^2$ for the valence bands includes the single-particle part $\tilde{H}_{\text{eff}}$ shown in Eqs. (9) and (10), and the interaction part $\mathcal{H}_{\text{int}}$ in Eq. (11).

Motivated by the recent breakthroughs of realizing FCIs in undriven $tMoTe_2$ at twist angles near 4°,[50–53] we consider the possibility of Floquet FCIs resulting from the topology of Floquet bands and the electron–electron interactions, as well as the evolution of Floquet FCIs during the band crossing in Fig. 2. Because we consider the off-resonant high-frequency light driving, we expect that the properties of the driven system can be well captured by the effective many-body Floquet Hamiltonian.[36–38,54] Therefore, we seek the signatures of Floquet FCIs from the eigenstates and spectrum of the effective many-body Floquet Hamiltonian using exact diagonalization. The specific occupation of Floquet bands required by Floquet FCIs could be realized by adiabatically increasing the CPL strength in an isolated Floquet system.[54,55] We adopt the model parameters of $tMoTe_2$ provided by first-principles calculations in Ref. [56] for twist angles near 4°: $(V, w, \psi, m^*) = (20.8\,\text{meV}, -23.8\,\text{meV}, -107.7°, 0.6m_e)$ and focus on $\theta = 3.7°$. For such a set of parameters, the Chern numbers of the top and second Floquet valence bands in valley + are +1 and −1, respectively. The Chern numbers of Floquet valence bands in the other valley are opposite, as in the undriven case. We set $d = 100\,\text{Å}$ and $\epsilon_{\text{r}} = 10$, where signatures of static FCIs at hole filling $\nu_{\text{h}} = 2/3$ were found in numerical simulations of undriven $tMoTe_2$.[57]

Considering that the static FCIs in undriven $tMoTe_2$ were observed in the hole-doped valence bands, we will also work in the hole picture for the convenience of comparing undriven and driven systems. After the particle–hole transformation, we can express the entire many-body Floquet Hamiltonian in the basis $|\boldsymbol{k}, \xi, n\rangle$ of hole bands as

$$\begin{aligned}\tilde{H}_{\text{eff}}^{\text{mb}} =& -\sum_{\boldsymbol{k}}^{\text{MBZ}}\sum_{\xi}\sum_{n} E_{\xi,n}(\boldsymbol{k})\gamma^\dagger_{\boldsymbol{k},\xi,n}\gamma_{\boldsymbol{k},\xi,n} \\ &+ \sum_{\{\boldsymbol{k}_i\}}^{\text{MBZ}}\sum_{\xi,\xi'}\sum_{\{n_i\}} V^{\xi\xi'}_{\{\boldsymbol{k}_i\}\{n_i\}}\gamma^\dagger_{\boldsymbol{k}_1,\xi,n_1}\gamma^\dagger_{\boldsymbol{k}_2,\xi',n_2} \\ &\times \gamma_{\boldsymbol{k}_3,\xi',n_3}\gamma_{\boldsymbol{k}_4,\xi,n_4},\end{aligned} \tag{13}$$

where all wave vectors are restricted in the moiré Brillouin zone (MBZ), $\gamma^\dagger_{\boldsymbol{k},\xi,n}(\gamma_{\boldsymbol{k},\xi,n})$ is the operator creating (annihilating) a hole with wave vector $\boldsymbol{k}$ in the Floquet valence band n of valley ξ, and the quasienergy of holes is the negative of electron quasienergy $E_{\xi,n}(\boldsymbol{k})$ obtained by diagonalizing the single-particle part $\tilde{H}_{\text{eff}}$. The interaction matrix element

$$\begin{aligned}V^{\xi\xi'}_{\{\boldsymbol{k}_i\}\{n_i\}} =& \frac{1}{2}\delta'_{\boldsymbol{k}_1+\boldsymbol{k}_2,\boldsymbol{k}_3+\boldsymbol{k}_4}\sum_{\boldsymbol{G}} V(\boldsymbol{k}_1-\boldsymbol{k}_4+\boldsymbol{G}) \\ &\times M_{\xi,n_1,n_2}(\boldsymbol{k}_1,\boldsymbol{k}_4-\boldsymbol{G}) \\ &\times M_{\xi,n_2,n_3}(\boldsymbol{k}_2,\boldsymbol{k}_3+\boldsymbol{G}+\delta\boldsymbol{G}),\end{aligned} \tag{14}$$

where δ' is the periodic Kronecker delta function with the period of MBZ reciprocal lattice vector $\boldsymbol{G}$, $M_{\xi,n,n'}(\boldsymbol{k},\boldsymbol{k}') = \langle u_{\xi,n}(\boldsymbol{k})|u_{\xi,n'}(\boldsymbol{k}')\rangle$ with $|u_{\xi,n}(\boldsymbol{k})\rangle$ the periodic part of the eigenstate of $\tilde{H}_{\text{eff}}$, and $\delta\boldsymbol{G} = \boldsymbol{k}_1 + \boldsymbol{k}_2 - \boldsymbol{k}_3 - \boldsymbol{k}_4$.

We will deal with finite periodic systems of N holes on the torus, so that each energy level has a well-defined many-body momentum K. We choose the tilted

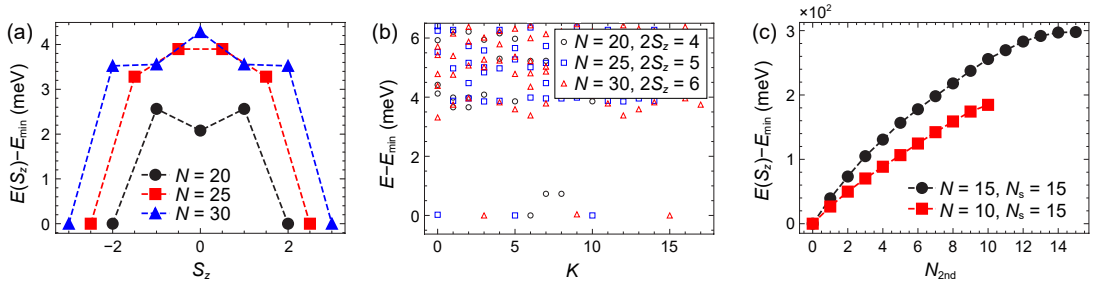

Fig. 3. Results for undriven $tMoTe_2$ at $\nu_h = 5/3$, with $N = 20$, 25, and 30 holes. (a) The lowest eigen-energy in each S_z sector. (b) The many-body spectra in the $2S_z = 4$, 5, and 6 sectors. (c) Dependence of the ground energy at $\nu_h = 1$ and $\nu_h = 2/3$ on the redistribution of holes between the top two valence bands, with the valley polarization imposed.

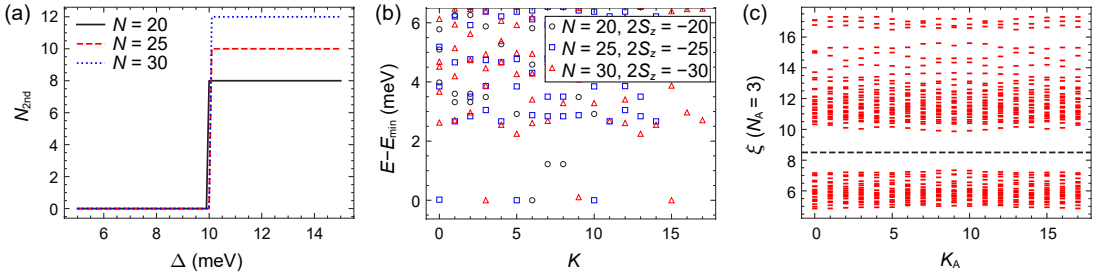

Fig. 4. Results for CPL-driven $tMoTe_2$ at $\nu_h = 5/3$, with $N = 20$, 25, and 30 holes. (a) The distribution of holes between the first Floquet valence band in valley + and the second Floquet valence band in valley − for different driving intensity Δ. N_{2nd} indicates the number of holes occupying the second Floquet valence band in valley −. (b) The low-energy spectrum at hole filling 5/3 in valley −. We choose $\Delta = 12$ meV. (c) The particle entanglement spectrum for 12 holes in the second Floquet band of valley − at $\nu_h = 2/3$, after the particle–hole transformation and choosing $N_A = 3$. There are 330 levels below the dashed line.

geometry [58,59] to make the samples as isotropic as possible. Because the number of holes N_ξ in each valley ξ is a good quantum number of Eq. (13), many-body eigenstates can be assigned with a z-direction pseudospin $S_z = (N_+ - N_-)/2$ as well. We are interested in the many-body physics during the crossing between the Floquet bands in opposite valleys. Therefore, we consider the hole filling at $\nu_h = 5/3$, where holes have to occupy both valleys.

Before investigating the driven system, we would like to characterize the many-body phase at this filling in the undriven system ($\Delta = 0$). For numerical efficiency, we first keep the top valence band in each valley and project the many-body Hamiltonian to these two bands. For all system sizes by us, we always find that the valley distribution of holes in the ground state is either $\nu_{h,+} = 1, \nu_{h,-} = 2/3$ or $\nu_{h,+} = 2/3, \nu_{h,-} = 1$, as shown in Fig. 3(a). These two energetically degenerate distributions correspond to $2S_z = \pm N/5$. The low-energy spectra in these S_z sectors demonstrate approximate three-fold degeneracy [Fig. 3(b)], which is striking evidence of the Laughlin-type FCI. Notably, signatures of FCIs at $\nu_h = 5/3$ were recently reported using transient optical spectroscopy. [60] Keeping two bands per valley exceeds our computational capability. However, for valley polarized undriven systems at either $\nu_h = 1$ or $\nu_h = 2/3$, we observe the ground energy increasing with N_{2nd}, the number of holes allowed to occupy the second valence band [Fig. 3(c)]. We hence argue that the mixing between the top two valence bands will not completely destroy the $\nu_h = 5/3$ FCIs shown in Fig. 3(b).

Next, we consider the driven $tMoTe_2$. After the CPL driving is turned on, the effective mass in $\tilde{H}_{eff}$ in the two valleys becomes different. Moreover, the electron's Floquet bands gain a negative (positive) quasienergy shift in valleys $\xi = +$ and $-$, respectively. Therefore, in the effective static system described by the many-body Floquet Hamiltonian $\tilde{H}^{mb}_{eff}$, the degeneracy at $\nu_h = 5/3$ between the $2S_z = \pm N/5$ sectors in the undriven system is broken. For very small driving intensity Δ, the Floquet FCI with $\nu_{h,+} = 2/3, \nu_{h,-} = 1$ configuration is selected as the ground state of $\tilde{H}^{mb}_{eff}$, because holes tend to occupy states with higher electron quasienergy. With the increase of Δ, the quasienergies of the top Floquet valence band in valley + become closer to that of the second Floquet valence band in valley −, as shown in Fig. 2. In this case, holes may redistribute among the two valleys.

To study this redistribution of holes in the ground state of $\tilde{H}^{mb}_{eff}$, we assume that the holes only occupy the top valence band in each valley in the undriven limit. Furthermore, because the second Floquet valence band in valley + and the top Floquet valence band in valley − are well separated from the other two crossing bands, we assume that they are not relevant to the redistribution of holes induced by the CPL, namely, the hole fillings in these two bands remain at 0 and 1 during the band crossing, respectively. Then we reach a simplified model of band crossing, consisting of the top Floquet valence band in valley + and the second Floquet valence band in valley −. These two bands are occupied at hole fillings 2/3 and 0 in the limit of $\Delta = 0$, respectively. In Fig. 4(a), we present the number

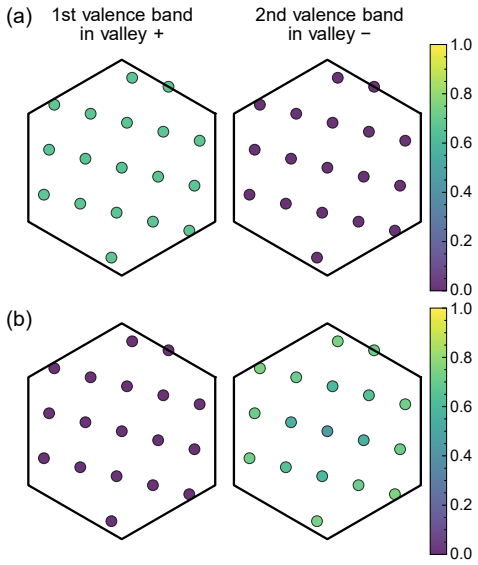

Fig. 5. The hole occupation number in the MBZ for the first Floquet valence band in valley + and the second Floquet valence band in valley − when (a) $\Delta = 5\,\text{meV}$ and (b) $\Delta = 12\,\text{meV}$. The finite system includes 18 moiré unit cells.

of holes occupying the second valence band in valley − as a function of Δ after the CPL driving is turned on. There is a clear transition at $\Delta_c \approx 10\,\text{meV}$, where all holes in the top Floquet valence band of valley + move to the second Floquet valence band of valley − (the number of holes occupying the top valence band in valley + is $2N/5$ in the limit of $\Delta = 0$). In this case, the distribution of holes becomes $\nu_{h,+} = 0, \nu_{h,-} = 5/3$ (the fully filled top Floquet valence band in valley − is included). The occupations of holes in the MBZ before and after the transition are displayed in Fig. 5.

After the transition, we project $\tilde{H}^{\text{mb}}_{\text{eff}}$ to the top two Floquet valence bands in valley −. At hole filling 5/3, we observe a three-fold ground-state degeneracy in the quasienergy spectrum, as shown in Fig. 4(b). We further compute the particle entanglement spectrum (PES) [32] for the particle–hole conjugate of the three ground states projected to the second Floquet valence band in valley −. There is a clear gap in the PES, the number of levels below which matches the expectation for the $\nu = 1/3$ Laughlin state [Fig. 4(c)]. These results point to the $\nu_h = 1 + 2/3$ Laughlin-type Floquet FCI fully polarized in valley −, where the second Floquet valence band is partially occupied at $\nu_h = 2/3$. By contrast, the Laughlin-type Floquet FCI at weak driving intensity ($\nu_{h,+} = 2/3, \nu_{h,-} = 1$) is not valley polarized, with hole occupations in both valleys. The valley polarized $\nu_h = 5/3$ Floquet FCI at strong driving intensity does not have a counterpart in undriven systems because of the energy degeneracy of static bands in two valleys.

5. Conclusions and Discussions. In this work, we have investigated the effect of CPL on twisted bilayer $MoTe_2$. We derive the single-particle Floquet Hamiltonian in the high-frequency limit up to the order of $1/\Omega^2$, using the full Dirac model involving both valence and conduction bands of monolayer $MoTe_2$. This Floquet Hamiltonian can be further simplified by integrating out the conduction band via Schrieffer–Wolff transformation, resulting in a free-electron model where the time-reversal symmetry is explicitly broken at the order of $1/\Omega$. Such a symmetry breaking effect is hidden if one starts from a free-electron model at the beginning to derive the Floquet Hamiltonian. Therefore, our results highlight the necessity of including the conduction band contribution when studying the Floquet problems of $tMoTe_2$ and other semiconductor moiré materials even if the static band gap is large.

We also explore the many-body physics of the driven $tMoTe_2$ at hole filling $\nu_h = 5/3$ during the intervalley band crossing induced by the CPL. Using the effective many-body Floquet Hamiltonian, we find numerical evidence of Laughlin-type Floquet FCIs and their valley transition with increasing CPL strength. It is possible to realize the required occupation of Floquet bands by adiabatically increasing the CPL strength. The timescale needed to achieve such an adiabatic preparation could be very short (a few driving periods), [55] while the lifetime of the resulting prethermal steady state grows exponentially with increasing driving frequency. [61] For the high-frequency off-resonant driving focused in this work, we expect that the many-body physics extracted from the effective Floquet Hamiltonian well describes the properties of the non-equilibrium system. We note that the light-induced anomalous Hall effect, i.e., the Floquet integer Chern insulator has been observed experimentally. [62] It will be exciting progress if the Floquet FCIs can be detected in experiments.

In the future, it would be interesting to derive the effective Floquet Hamiltonian and study the many-body physics under the driving of a longitudinal light. It is also worth exploring the Floquet physics in other semiconductor moiré materials, like in twisted bilayer WSe_2.

Acknowledgements. This work was supported by the National Natural Science Foundation of China (Grant Nos. 12374149 and 12350403) and the National Key Research and Development Program of China (Grant No. 2020YFA0309200).

References

[1] Castro A, De Giovannini U, Sato S A, Hübener H, and Rubio A 2022 *Phys. Rev. Res.* **4** 033213
[2] Khemani V, Lazarides A, Moessner R, and Sondhi S L 2016 *Phys. Rev. Lett.* **116** 250401
[3] Potter A C, Morimoto T, and Vishwanath A 2016 *Phys. Rev. X* **6** 041001
[4] Yao N Y, Potter A C, Potirniche I D, and Vishwanath A 2017 *Phys. Rev. Lett.* **118** 030401
[5] Potirniche I D, Potter A C, Schleier-Smith M, Vishwanath A, and Yao N Y 2017 *Phys. Rev. Lett.* **119** 123601
[6] Lerose A, Marino J, Gambassi A, and Silva A 2019 *Phys. Rev. B* **100** 104306
[7] Eckardt A and Anisimovas E 2015 *New J. Phys.* **17** 093039
[8] Bukov M, D'Alessio L, and Polkovnikov A 2015 *Adv. Phys.* **64** 139
[9] Mikami T, Kitamura S, Yasuda K, Tsuji N, Oka T, and Aoki H 2016 *Phys. Rev. B* **93** 144307

[10] Rodriguez-Vega M, Vogl M, and Fiete G A 2021 *Ann. Phys.* **435** 168434
[11] Vajna S, Klobas K, Prosen T, and Polkovnikov A 2018 *Phys. Rev. Lett.* **120** 200607
[12] Vogl M, Rodriguez-Vega M, and Fiete G A 2020 *Phys. Rev. B* **101** 235411
[13] Vogl M, Laurell P, Barr A D, and Fiete G A 2019 *Phys. Rev. A* **100** 012132
[14] Verdeny A, Mielke A, and Mintert F 2013 *Phys. Rev. Lett.* **111** 175301
[15] Vogl M, Laurell P, Barr A D, and Fiete G A 2019 *Phys. Rev. X* **9** 021037
[16] Oka T and Aoki H 2009 *Phys. Rev. B* **79** 081406
[17] Oka T and Kitamura S 2019 *Annu. Rev. Condens. Matter Phys.* **10** 387
[18] Tsuji N, Oka T, and Aoki H 2008 *Phys. Rev. B* **78** 235124
[19] Tsuji N, Oka T, and Aoki H 2009 *Phys. Rev. Lett.* **103** 047403
[20] Katz O, Refael G, and Lindner N H 2020 *Phys. Rev. B* **102** 155123
[21] Topp G E, Jotzu G, McIver J W, Xian L, Rubio A, and Sentef M A 2019 *Phys. Rev. Research* **1** 023031
[22] Li Y, Fertig H A, and Seradjeh B 2020 *Phys. Rev. Research* **2** 043275
[23] Ikeda T N 2020 *Phys. Rev. Res.* **2** 032015
[24] Vogl M, Rodriguez-Vega M, and Fiete G A 2020 *Phys. Rev. B* **101** 241408
[25] Rodriguez-Vega M, Vogl M, and Fiete G A 2020 *Phys. Rev. Res.* **2** 033494
[26] Assi I A, LeBlanc J P F, Rodriguez-Vega M, Bahlouli H, and Vogl M 2021 *Phys. Rev. B* **104** 195429
[27] Lu M, Zeng J, Liu H, Gao J H, and Xie X C 2021 *Phys. Rev. B* **103** 195146
[28] Sun K, Gu Z, Katsura H, and Das Sarma S 2011 *Phys. Rev. Lett.* **106** 236803
[29] Tang E, Mei J W, and Wen X G 2011 *Phys. Rev. Lett.* **106** 236802
[30] Neupert T, Santos L, Chamon C, and Mudry C 2011 *Phys. Rev. Lett.* **106** 236804
[31] Sheng D N, Gu Z C, Sun K, and Sheng L 2011 *Nat. Commun.* **2** 389
[32] Regnault N and Bernevig B A 2011 *Phys. Rev. X* **1** 021014
[33] Parameswaran S A, Roy R, and Sondhi S L 2013 *CR Phys.* **14** 816
[34] Bergholtz E J and Liu Z 2013 *Int. J. Mod. Phys. B* **27** 1330017
[35] Liu Z and Bergholtz E J 2024 *Encyclopedia of Condensed Matter Physics (Second Edition)* (Oxford: Academic Press) pp. 515–538
[36] Grushin A G, Gómez-León Á, and Neupert T 2014 *Phys. Rev. Lett.* **112** 156801
[37] Anisimovas E, Žlabys G, Anderson B M, Juzeliūnas G, and Eckardt A 2015 *Phys. Rev. B* **91** 245135
[38] Hu P S, Zhou Y H, and Liu Z 2023 *SciPost Phys.* **15** 148
[39] Dong J, Lin Z, Gu B L, and Duan W 2024 *Phys. Rev. B* **110** 144444
[40] Qin F, Chen R, and Lee C H 2024 *Commun. Phys.* **7** 368
[41] Wu F, Lovorn T, Tutuc E, and MacDonald A H 2018 *Phys. Rev. Lett.* **121** 026402
[42] Zhan Z, Zhang Y, Lv P, Zhong H, Yu G, Guinea F, Silva-Guillén J Á, and Yuan S 2020 *Phys. Rev. B* **102** 241106
[43] Devakul T, Crépel V, Zhang Y, and Fu L 2021 *Nat. Commun.* **12** 6730
[44] Vogl M, Rodriguez-Vega M, Flebus B, MacDonald A H, and Fiete G A 2021 *Phys. Rev. B* **103** 014310
[45] Xiao D, Liu G B, Feng W, Xu X, and Yao W 2012 *Phys. Rev. Lett.* **108** 196802
[46] Su Y, Li H, Zhang C, Sun K, and Lin S Z 2022 *Phys. Rev. Res.* **4** L032024
[47] Wu F, Lovorn T, Tutuc E, Martin I, and MacDonald A H 2019 *Phys. Rev. Lett.* **122** 086402
[48] Rahav S, Gilary I, and Fishman S 2003 *Phys. Rev. A* **68** 013820
[49] Goldman N and Dalibard J 2014 *Phys. Rev. X* **4** 031027
[50] Park H, Cai J, Anderson E *et al.* 2023 *Nature* **622** 74
[51] Zeng Y, Xia Z, Kang K, Zhu J, Knüppel P, Vaswani C, Watanabe K, Taniguchi T, Mak K F, and Shan J 2023 *Nature* **622** 69
[52] Cai J, Anderson E, Wang C *et al.* 2023 *Nature* **622** 63
[53] Xu F, Sun Z, Jia T, Liu C, Xu C, Li C, Gu Y, Watanabe K, Taniguchi T, Tong B, Jia J, Shi Z, Jiang S, Zhang Y, Liu X, and Li T 2023 *Phys. Rev. X* **13** 031037
[54] Kitagawa T, Oka T, Brataas A, Fu L, and Demler E 2011 *Phys. Rev. B* **84** 235108
[55] Dahlhaus J P, Fregoso B M, and Moore J E 2015 *Phys. Rev. Lett.* **114** 246802
[56] Wang C, Zhang X W, Liu X, He Y, Xu X, Ran Y, Cao T, and Xiao D 2024 *Phys. Rev. Lett.* **132** 036501
[57] Yu J, Herzog-Arbeitman J, Wang M, Vafek O, Bernevig B A, and Regnault N 2024 *Phys. Rev. B* **109** 045147
[58] Läuchli A M, Liu Z, Bergholtz E J, and Moessner R 2013 *Phys. Rev. Lett.* **111** 126802
[59] Repellin C, Bernevig B A, and Regnault N 2014 *Phys. Rev. B* **90** 245401
[60] Wang Y, Choe J, Anderson E *et al.* 2025 *Nature* **641** 1149
[61] Abanin D A, De Roeck W, Ho W W, and Huveneers F 2017 *Phys. Rev. B* **95** 014112
[62] McIver J W, Schulte B, Stein F U, Matsuyama T, Jotzu G, Meier G, and Cavalleri A 2020 *Nat. Phys.* **16** 38